Trends in advanced sciences and technology

Trends in Advanced Sciences and Technology

Volume 1 Article 19

2024

Analysis of Second-Order Dynamic Coefficients for Herringbone Grooved Hydrodynamic Thrust Bearings Considering Misalignment

Elsayed K. Elsayed
Department of Mechanical Design, Faculty of Engineering, Mataria, Helwan University, P.O. Box 11718, Helmeiat-Elzaton, Cairo, Egypt

Tamer.A. El-Sayed
Department of Mechanical Design, Faculty of Engineering, Mataria, Helwan University, P.O. Box 11718, Helmeiat-Elzaton, Cairo, Egypt, tamer_alsayed@m-eng.helwan.edu.eg

Hussein Sayed
Department of Mechanical Design, Faculty of Engineering, Mataria, Helwan University, P.O. Box 11718, Helmeiat-Elzaton, Cairo, Egypt

How to Cite This Article

Elsayed, Elsayed K.; El-Sayed, Tamer.A.; and Sayed, Hussein (2024) "Analysis of Second-Order Dynamic Coefficients for Herringbone Grooved Hydrodynamic Thrust Bearings Considering Misalignment," *Trends in advanced sciences and technology*: Vol. 1, Article 19.
DOI: 10.62537/2974-444X.1020
Available at: https://tast.researchcommons.org/journal/vol1/iss1/19

ORIGINAL STUDY

Analysis of Second-order Dynamic Coefficients for Herringbone-grooved Hydrodynamic Thrust Bearings Considering Misalignment

Elsayed Khodry Elsayed [a], Tamer Ahmed El-Sayed [a,b,c,*], Hussein Sayed [a]

[a] Department of Mechanical Design, Faculty of Engineering, Mataria, Helwan University, Egypt
[b] Centre for Applied Dynamics Research, School of Engineering, University of Aberdeen, Aberdeen, UK
[c] School of Engineering, University of Hertfordshire Hosted by Global Academic Foundation, Cairo, Egypt

Abstract

Background: **A herringbone-grooved hydrodynamic thrust bearing is a specialized type of bearing designed to support axial loads in rotating machinery. It is commonly used in turbines, compressors, and pumps. It uses a hydrodynamic lubrication mechanism to reduce friction and wear between the rotating and stationary parts.**

Methods: **In this paper, a second-order dynamic analysis for the herringbone-grooved thrust bearing based on the finite perturbation approach is performed. The Reynolds equation, expressed in polar coordinates, was differentiated to analyze small perturbations from the equilibrium state. This process yielded the first-order equation and then the second-order equation describing these perturbations. The Reynolds equation and its perturbed equations were solved using the finite difference approach and the over-relation method to get the static and dynamic parameters of the thrust bearing. A three degree of freedom model was used in this study to get the bearing dynamic coefficients (linear in z, rotation in x and y).**

Results: **This study investigates the effect of different operating conditions on bearing coefficients, such as the misalignment angle and the rotation speed. The results are verified with the previous literature, and perturbation analysis with three different methods is conducted to calculate the bearing force and moments for model validation and the effect of misalignment angle and rotational speed on dynamic coefficients. The results showed that, when the rotor is aligned, the max pressure is 9.29 bar and when the rotor tilted by 0.24×10^{-3} rad, the max pressure increases to 69.44 bar. This indicates that with increasing the misalignment angle the pressure increases causing an increase in the load-carrying capacity and bearing coefficients.**

Conclusion: **This research demonstrates that using the finite perturbation method to evaluate the first-order and second-order bearing coefficients of a herringbone-grooved thrust bearing can enhance the accuracy of the thrust bearing model. The study also underscores the substantial impact of misalignment and rotational speed on the dynamic coefficients of the thrust bearing. The findings presented in this work offer valuable data that can be leveraged as input for rotor dynamics analyses in high-speed rotating equipment.**

Keywords: Dynamic coefficients, Finite difference method, Herringbone thrust bearing, Perturbation analysis, Second-order analysis

1. Introduction

Herringbone-grooved thrust bearings are crucial components in various applications like high-speed transmissions and rotor systems. Research has focused on optimizing these bearings for enhanced load capacity, stability, and performance (Ran *et al.*, 2022; Schlums *et al.*, 2022; Wang *et al.*, 2022; Wang & Lin, 2022; Yu *et al.*, 2021). Research studies have investigated various factors,

Received 8 June 2024; revised 10 August 2024; accepted 31 August 2024.
Available online 10 October 2024

* Corresponding author at: Department of Mechanical Design, Faculty of Engineering, Mataria, Helwan University, PO Box 11718, Helmeiat-Elzaton, Cairo, Egypt.
E-mail address: tamer_alsayed@m-eng.helwan.edu.eg (T.A. El-Sayed).

https://doi.org/10.62537/2974-444X.1020

including groove parameters, misalignment effects, and lubrication mechanisms, to enhance the design and functionality of bearings. Computational fluid dynamics models have been utilized to analyze pressure distributions, temperature effects, and flow regimes within these bearings, offering insights into their microhydrodynamic behavior. Investigations have explored the impact of different groove configurations on load capacity, temperature variations, and eccentricity ratios, providing valuable guidelines for designing efficient herringbone-grooved thrust bearings suitable for diverse operating conditions.

1.1. Analysis of herringbone-grooved thrust bearing performance

Analyzing the performance of herringbone-grooved thrust bearings involves a comprehensive evaluation of various factors affecting their functionality and efficiency such as load capacity, friction characteristics, lubrication effectiveness, and comparative analysis. By conducting a thorough analysis of these factors and potentially others specific to the herringbone-grooved thrust bearings, engineers can gain valuable insights into the bearing's performance characteristics and make informed decisions to improve its efficiency and reliability in various applications. Numerous researchers have put forth various approaches to study the performance parameters of the herringbone-grooved thrust bearing under different geometrical and

Nomenclature

C	nominal film thickness (m)
$C_{\eta\zeta}$	first-order damping coefficient $\zeta, \eta = z, \theta_x, \theta_y, \dot{z}, \dot{\theta_x}, \dot{\theta_y}$
$C_{\eta\zeta\gamma}$	second-order damping coefficient $\zeta, \eta, \gamma = z, \theta_x, \theta_y, \dot{z}, \dot{\theta_x}, \dot{\theta_y}$
F_z	axial force (N)
h_g	groove depth (m)
$K_{\eta\zeta}$	first-order stiffness coefficients $\zeta, \eta = z, \theta_x, \theta_y$
$K_{\eta\zeta\gamma}$	second-order stiffness coefficients $\zeta, \eta, \gamma = z, \theta_x, \theta_y$
M_x, M_y	bearing moments (Nm)
n	rotating speed (rpm)
p	fluid film pressure (N/m^2)
r	radial coordinate
r_1	bearing inner radius (m)
r_2	bearing outer radius (m)
t	time (s)
v_θ	shaft mean speed (m/s); $(r_1/2 + r_2/2)*\omega$
x, y, z	Cartesian coordinates
Δz	axial displacement (m)
$\Delta \dot{z}$	axial velocity (m/s)
θ	circumferential coordinate
$\theta_{x_0}, \theta_{y_0}$	misalignment angle in x and y directions (rad)
$\Delta\theta_x, \Delta\theta_y$	angular displacement in x and y directions (rad/s)
$\Delta\dot{\theta}_x, \Delta\dot{\theta}_y$	angular velocity in x and y directions (rad/s^2)
μ	viscosity (N.s/m^2)
ω	Angular velocity (rad/s)

Subscripts

0	Nonlinear

Superscripts

f	first order
s	second order

Table 1. Pervious literature aims and important findings related to the performance analysis of grooved thrust bearings.

References	Research aim	Important findings
Lehn and Schweizer (2016)	Solve generalized Reynolds equation for double-sided spiral groove thrust bearing. Validate with CFD calculations	One-sided SGB outperforms double-sided SGB. Double-sided SGB has a 12% lower load capacity. 42% difference in minimal friction coefficient
Xiang *et al.* (2019)	Examine the lubrication effectiveness of micro-grooved journal bearings. Analyze different groove distributions: straight, spiral, herringbone	Herringbone groove has the highest load capacity. Spiral groove shows the least load capacity and variability
Luan *et al.* (2023)	Study herringbone groove geometry and inlet taper height on gas foil HGBT	Herringbone bearing groove parameters identified. Enhanced performance of gas foil thrust bearings suggested
Hu and Meng (2019); Zhou *et al.* (2023)	Analyze the tribological behavior of SGBs with a mixed lubrication model. Evaluate performance under varying conditions	Groove width ratio >0.2 raises friction and contact load. Optimal spiral angle recommended at 400 to reduce friction
Agrawal and Sharma (2023)	Analyze the efficiency of microgrooved hybrid spherical thrust bearing. Consider non-Newtonian lubricant properties	Microgrooves improve hybrid bearing efficiency. Performance influenced by microgroove geometry
Tang *et al.* (2022)	Analyze lubrication in journal-thrust coupled microgroove bearings. Compare five microgroove shapes	Left triangle microgroove shape offers the best performance. Ideal thrust bearing pad inclination angle: 0.010
Dai *et al.* (2022)	Develop dynamic model to study time-varying mixed lubrication in bearings	Optimal microgroove shape depends on depth. The influence of the coupling hydrodynamic on the time-varying mixed lubrication is strengthened with increasing microgroove depth

CFD, computational fluid dynamics; SGB, spiral grooved bearing.

operating conditions due to its importance in the dynamic analysis of rotor-bearing systems. Table 1 summarizes the research aims and the most important findings of some previous literature that focused on studying the performance of grooved thrust bearings.

1.2. Calculations of bearing dynamic coefficients

Calculating hydrodynamic bearing dynamic coefficients is a critical step in ensuring the reliable and efficient operation of rotating machinery. Accurate prediction of system behavior, design optimization, and fault diagnosis all rely on this information. Many researchers have studied the dynamic characteristics of thrust bearings and analyzed the damping and stiffness coefficients at different operating conditions and shapes of thrust bearings. Table 2 shows some of the previous studies that studied the dynamic coefficients of thrust bearings, and the most important results obtained.

There is a lack of knowledge in dealing with the herringbone-grooved thrust bearing in calculating the dynamic coefficients and the effect of the various operating factors on those parameters, affecting the dynamic performance of the rotor-bearing system. As a result, in the present research, a higher order analysis was used to determine the dynamic coefficients of a herringbone thrust bearing up to the second order with three degrees of freedom model considering the misalignment effect, which is the novel aspect of this work. The researchers built upon a solution method from a previous reference (Jang & Kim, 1999), extending it by incorporating the infinitesimal perturbation technique alongside the finite difference method for pressure integration. By introducing small perturbation values, the bearing coefficients for small displacements $(\Delta z, \Delta\theta_x, \Delta\theta_y)$ and velocities $(\Delta\dot{z}, \Delta\dot{\theta}_x, \Delta\dot{\theta}_y)$ relative to the shaft's

Table 2. Previous studies on bearing dynamic coefficients.

References	Research aim	Important findings
Yu *et al.* (2017)	Investigate static and dynamic characteristics of herringbone-grooved air thrust bearings. Use finite difference and finite volume methods to solve the Reynolds equation	Herringbone-grooved thrust bearings support greater loads than hydrostatic ones. Increased air consumption at high compressibility numbers. Stability issues at high rotational speeds; deeper grooves improve stability
Elsayed *et al.* (2023)	Determine dynamic coefficients of a 3-DOF model for inclined pad thrust bearings. Use infinitesimal perturbation approach and finite difference method	Operating conditions such as misalignment angle, rotational speed, and fluid film thickness affect bearing coefficients
Xiang and Han (2020), Xiang *et al.* (2020, 2021a, 2021b)	Study the effect of misalignment and tiny axial vibrations on misaligned journal-thrust micro-groove-coupled bearings under water lubrication	Coupled bearing enhances lubrication performance of both journal and thrust bearings. Axial microvibrations cause periodic load capacity fluctuations
Lin *et al.* (2020, 2022), Zhang *et al.* (2020)	Simulate lubrication of high-speed thrust bearings with spiral grooves under water, considering liquid and gas flow and tiny air bubbles	Cavitation effect increases direct stiffness coefficients. Cross-stiffness and damping coefficients are minimally affected by cavitation
Sahu *et al.* (2006)	Determine steady-state and stability properties of herringbone-grooved journal bearings, considering thermal effects. Calculate oil film stiffness and damping coefficients using the first-order perturbation technique	Herringbone-grooved journal bearings are more stable with lower end leakage. They have greater load-carrying capacity compared with plain journal bearings
Jang and Lee (2006), Jang *et al.* (2005), Jang and Yoon (2003)	Calculate stiffness and damping coefficients of a coupled journal and thrust bearing in a rotor system using the 5-DOF model. Employ the finite element method	Mathematical perturbation method is more computationally efficient and stable than physical perturbation
Oh and Rhim (2001)	Analyze the bearing system combining herringbone-grooved journal bearing and spiral-grooved thrust bearing using the 3-DOF model. Use the perturbation method to determine dynamic coefficients	Identified unstable system state based on geometric parameters. Suggested adjustments to parameters to prevent instability
El-Sayed and Sayed (2022), Sayed and El-Sayed (2022a, 2022b), Ahmed *et al.* (2023), El-Sayed *et al.* (2023), Sayed *et al.* (2023), Ahmed *et al.* (2024)	Calculate nonlinear bearing coefficients for journal bearings using the Taylor expansion method and finite perturbation. Investigate second-order and third-order bearing coefficients under various conditions	Third-order coefficients from Taylor's expansion are useful in rotor-bearing dynamics. Analysis accuracy is low when the journal close to the limit circle; however; multidimensional fitting can overcome this limitation

DOF, degree of freedom.

equilibrium position are evaluated. The investigation also explored the impact of shaft misalignment and rotational speed on dynamic coefficients of the bearing.

2. Theoretical analysis

In this section, the governing equations that describe the pressure distribution and fluid film thickness in the system are introduced. To compute the pressure distribution and evaluate the load-carrying capacity, the finite difference method is used. By solving the equations on this discretized grid, the pressure distribution is computed, and subsequently, the load-carrying capacity of the system is evaluated. The infinitesimal perturbation approach is used to derive the first-order and second-order perturbed pressure equations, enabling the calculation of dynamic coefficients. The Reynolds equation is solved under several assumptions, including Newtonian fluid behavior, laminar flow, incompressible fluid, negligible inertia forces, negligible body forces, and thin film geometry. The structure parameters of the herringbone-grooved thrust bearing are shown in Fig. 1. The Reynolds equation that governs the pressure distribution for herringbone-grooved thrust bearing in a cylindrical coordinate can be written as follows:

$$\frac{\partial}{r\partial r}\left(\frac{rh^3}{12\mu}\frac{\partial p}{\partial r}\right)+\frac{1}{r}\frac{\partial}{\partial\theta}\left(\frac{h^3}{12\mu}\frac{\partial p}{r\partial\theta}\right)=\frac{v_\theta}{r}\frac{\partial h}{\partial\theta}+\frac{\partial h}{\partial t} \tag{1}$$

where p is the film pressure, h is the film thickness, r, θ are the radial and tangential coordinates, and μ, ω, t are the viscosity, angular velocity, and time, respectively. The static fluid film thickness can be shown as follows:

$$h_{static}=\begin{cases} C \text{ land area} \\ C+h_g \text{ groove area} \end{cases} \tag{2}$$

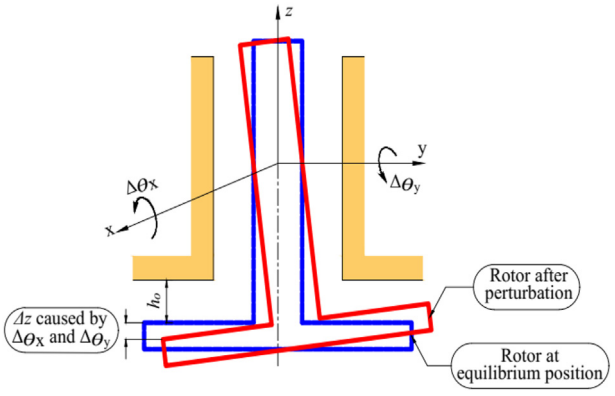

Fig. 2. Applied perturbations to the 3-DOF rotor-bearing model showing angular and axial perturbation. DOF, degree of freedom.

where C is the distance between the runner and the bearing pad and h_g is the groove depth as shown in Fig. 1.

$$h=h_0-r\Delta\theta_x\sin\theta+r\Delta\theta_y\cos\theta+\Delta z \tag{3}$$

A slight change in the runner's position (including a small movement sideways, Δz, and small tilts, $\Delta\theta_x$ and $\Delta\theta_y$) and a slight change in its speed (including a small sideways movement, $\Delta\dot{z}$, and small tilts, $\Delta\dot{\theta}_x$ and $\Delta\dot{\theta}_y$) disrupts its steady state. As shown in Fig. 2, this disruption affects the fluid film thickness between the bearing and the thrust collar, as described in the following equation:

The equilibrium position film thickness h_o is given by

$$h_o=h_{static}-r\theta_{x0}\sin\theta+r\theta_{y0}\cos\theta \tag{4}$$

Taking the derivative of Equation (3) yields the following expression:

$$\frac{\partial h}{\partial t}=-r\Delta\dot{\theta}_x\sin\theta+r\Delta\dot{\theta}_y\cos\theta+\Delta\dot{z} \tag{5}$$

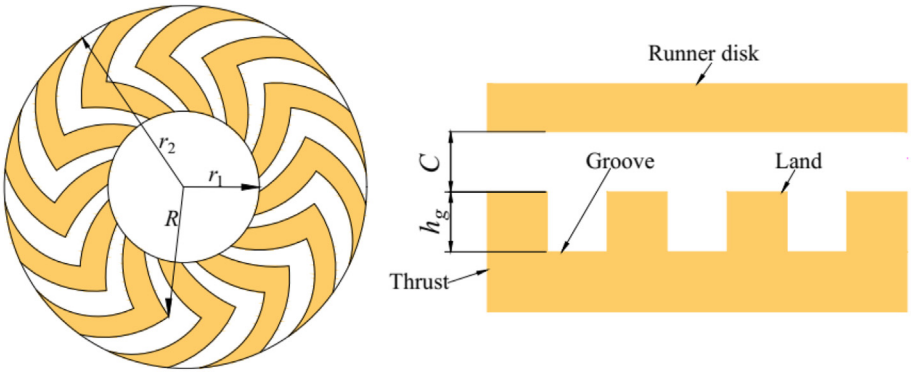

Fig. 1. Geometry and nomenclature of the herringbone-grooved thrust bearing.

A small disturbance in the fluid film leads to a corresponding change in pressure distribution. This perturbed pressure can be described by the following equation:

$$p = p_o + \sum_{\zeta} p_{\zeta}\Delta\zeta + \sum_{\dot{\zeta}} p_{\dot{\zeta}}\Delta\dot{\zeta} \tag{6}$$

where $\zeta = z, \theta_x, \theta_y$ and $\dot{\zeta} = \dot{z}, \dot{\theta}_x, \dot{\theta}_y$

Substituting Equations (3, 5, and 6) into the Reynolds equation (1) yields a system of six new equations, referred to as the "perturbed equations." These perturbed equations enable the calculation of the thrust bearing's damping and stiffness coefficients at the first-order approximation. The following equations illustrate the process of extracting these coefficients from the perturbed system:

$$\begin{aligned}&\left(\frac{3h^2h_{\zeta}}{12\mu r}+\frac{6hh_{\zeta}h_r}{12\mu}+\frac{3h^2h_{r\zeta}}{12\mu}\right)p_r+\left(\frac{h^3}{12\mu r}+\frac{3h^2h_r}{12\mu}\right)p_{r\zeta}\\&+\left(\frac{3h^2h_{\zeta}}{12\mu}\right)p_{rr}+\left(\frac{h^3}{12\mu}\right)p_{rr\zeta}+\left(\frac{6hh_{\zeta}h_{\theta}}{12\mu r^2}+\frac{3h^2h_{\theta\zeta}}{12\mu r^2}\right)p_{\theta}\\&+\left(\frac{3h^2h_{\theta}}{12\mu r^2}\right)p_{\theta\zeta}+\left(\frac{3h^2h_{\zeta}}{12\mu r^2}\right)p_{\theta\theta}+\left(\frac{h^3}{12\mu r^2}\right)p_{\theta\theta\zeta}=\frac{v_{\theta}}{r}h_{\theta\zeta}\end{aligned} \tag{7}$$

and

$$\begin{aligned}&\left(\frac{h^3}{12\mu r}+\frac{3h^2h_r}{12\mu}\right)p_{r\dot{\eta}}+\left(\frac{h^3}{12\mu r}\right)p_{rr\dot{\eta}}+\left(\frac{3h^2h_{\theta}}{12\mu r^2}\right)p_{\theta\dot{\eta}}\\&+\left(\frac{h^3}{12\mu r^2}\right)p_{\theta\theta\dot{\eta}}=h_{\eta}\end{aligned} \tag{8}$$

where $\zeta = z, \theta_x, \theta_y$ and $\dot{\eta} = \dot{z}, \dot{\theta}_x, \dot{\theta}_y$

$$p_r = \frac{\partial p}{\partial r}, p_{rr} = \frac{\partial^2 p}{\partial r^2}, p_{\theta} = \frac{\partial p}{\partial \theta}, p_{\theta\theta} = \frac{\partial^2 p}{\partial \theta^2}, h_r = \frac{\partial h}{\partial r} = -\theta_x \sin\theta + \theta_y \cos\theta$$

$h_{\theta} = \frac{\partial h}{\partial \theta} = -r\theta_{x0}\cos\theta - r\theta_{y0}\sin\theta$, for both land area and grooved areas.

2.1. Load-carrying capacity and dynamic coefficient calculations

To ascertain the forces exerted on the bearing, including the load-carrying capacity, reaction forces, and moments, the finite difference method is used to solve the Reynolds equation and its perturbed equations (Equations 1, 7, and 8). In this method, p_0 is calculated using Equation (1) at a zero rate of change in film thickness (denoted by $\partial h/\partial t = 0$):

$$F_o = \begin{Bmatrix} F_{z0} \\ M_{x0} \\ M_{y_0} \end{Bmatrix} = \iint_{r,\theta} \begin{Bmatrix} -p_o \\ p_o r\sin\theta \\ -p_o r\cos\theta \end{Bmatrix} r\mathrm{d}r\mathrm{d}\theta \tag{9}$$

The bearing force and moment can be calculated as follows:

$$\begin{Bmatrix} F_z^f \\ M_x^f \\ M_y^f \end{Bmatrix} = \iint_{r,\theta} \left\{ p_o + \sum_{\zeta} p_{\zeta}\Delta\zeta + \sum_{\dot{\zeta}} p_{\dot{\zeta}}\Delta\dot{\zeta} \right\} \times \begin{Bmatrix} -1 \\ r\sin\theta \\ -r\cos\theta \end{Bmatrix} r\mathrm{d}r\mathrm{d}\theta = F_o + K_{\eta\zeta}\begin{Bmatrix} \Delta z \\ \Delta\theta_x \\ \Delta\theta_y \end{Bmatrix} + C_{\eta\zeta}\begin{Bmatrix} \Delta\dot{z} \\ \Delta\dot{\theta}_x \\ \Delta\dot{\theta}_y \end{Bmatrix} \tag{10}$$

F represents the bearing's load-carrying capacity. $K_{\eta\zeta}$ and $C_{\eta\zeta}$ represent the bearing's stiffness and damping coefficients, respectively, in first order. These terms can be expressed mathematically as follows:

$$K_{\eta\zeta} = \begin{bmatrix} K_{zz} & K_{z\theta_x} & K_{z\theta_y} \\ K_{\theta_x z} & K_{\theta_x\theta_x} & K_{\theta_x\theta_y} \\ K_{\theta_y z} & K_{\theta_y\theta_x} & K_{\theta_y\theta_y} \end{bmatrix} = \iint_{r,\theta} \begin{Bmatrix} -1 \\ r\sin\theta \\ -r\cos\theta \end{Bmatrix} \times \left\{ p_z\, p_{\theta_x}\, p_{\theta_y} \right\} r\mathrm{d}r\mathrm{d}\theta \tag{11}$$

$$C_{\eta\zeta} = \begin{bmatrix} C_{zz} & C_{z\theta_x} & C_{z\theta_y} \\ C_{\theta_x z} & C_{\theta_x\theta_x} & C_{\theta_x\theta_y} \\ C_{\theta_y z} & C_{\theta_y\theta_x} & C_{\theta_y\theta_y} \end{bmatrix} = \iint_{r,\theta} \begin{Bmatrix} -1 \\ r\sin\theta \\ -r\cos\theta \end{Bmatrix} \times \left\{ p_{z\cdot}\, p_{\theta_x}\, p_{\theta_y} \right\} r\mathrm{d}r\mathrm{d}\theta \tag{12}$$

For which $K_{zz} = \partial F_z/\partial z$, $K_{z\theta_x} = \partial F_z/\partial\theta_x$, $K_{z\theta_y} = \partial F_z/\partial\theta_y$, $K_{\theta_x z} = \partial M_x/\partial z$, … and so on. And $C_{zz} = \partial F_z/\partial z\cdot$, $C_{z\theta_x} = \partial F_z/\partial\theta_x\cdot$, $C_{z\theta_y} = \partial F_z/\partial\theta_y\cdot$, $C_{\theta_x z} = \partial M_x/\partial z\cdot$, and so on.

To obtain the second-order dynamic behavior of the system, the perturbed pressure equations obtained from Equations (7 and 8) are differentiated with respect to these variables: (z, θ_x, θ_y, $\dot{z}$, $\dot{\theta}_x$, $\dot{\theta}_y$). This differentiation process yields the following second-order perturbed equations:

$$\left(\frac{6hh_\zeta h_\gamma}{12\mu r}+\frac{6h_\zeta h_\gamma h_r+6hh_\zeta h_{r\gamma}+6hh_\gamma h_{r\zeta}}{12\mu}\right)p_r$$
$$+\left(\frac{3h^2h_\zeta}{12\mu r}+\frac{6hh_\zeta h_r+3h^2h_{r\zeta}}{12\mu}\right)p_{r\gamma}$$
$$+\left(\frac{3h^2h_\gamma}{12\mu r}+\frac{6hh_\gamma h_r+3h^2h_{r\gamma}}{12\mu}\right)p_{r\zeta}$$
$$+\left(\frac{h^3}{12\mu r}+\frac{3h^2h_r}{12\mu}\right)p_{r\zeta\gamma}+\left(\frac{6hh_\zeta h_\gamma}{12\mu}\right)p_{rr}+\left(\frac{3h^2h_\zeta}{12\mu}\right)p_{rr\gamma}$$
$$+\left(\frac{3h^2h_\gamma}{12\mu}\right)p_{rr\zeta}+\left(\frac{h^3}{12\mu r}\right)p_{rr\zeta\gamma}$$
$$+\left(\frac{6h_\zeta h_\gamma h_\theta+6hh_\zeta h_{\theta\gamma}+6hh_\gamma h_{\theta\zeta}}{12\mu r^2}\right)p_\theta$$
$$+\left(\frac{6hh_\zeta h_\theta+3h^2h_{\theta\zeta}}{12\mu r^2}\right)p_{\theta\gamma}+\left(\frac{6hh_\gamma h_\theta+3h^2h_{\theta\gamma}}{12\mu r^2}\right)p_{\theta\zeta}$$
$$+\left(\frac{3h^2h_\theta}{12\mu r^2}\right)p_{\theta\zeta\gamma}+\left(\frac{6hh_\zeta h_\gamma}{12\mu r^2}\right)p_{\theta\theta}+\left(\frac{3h^2h_\zeta}{12\mu r^2}\right)p_{\theta\theta\gamma}$$
$$+\left(\frac{3h^2h_\gamma}{12\mu r^2}\right)p_{\theta\theta\zeta}+\left(\frac{h^3}{12\mu r^2}\right)p_{\theta\theta\zeta\gamma}=0 \tag{13}$$

and

$$\left(\frac{3h^2h_\zeta}{12\mu r}+\frac{6hh_\zeta h_r}{12\mu}+\frac{3h^2h_{r\zeta}}{12\mu}\right)p_{r\dot\gamma}+\left(\frac{h^3}{12\mu r}+\frac{3h^2h_r}{12\mu}\right)p_{r\zeta\dot\gamma}$$
$$+\left(\frac{3h^2h_\zeta}{12\mu}\right)p_{rr\dot\gamma}+\left(\frac{h^3}{12\mu}\right)p_{rr\zeta\dot\gamma}+\left(\frac{6hh_\zeta h_\theta}{12\mu r^2}+\frac{3h^2h_{\theta\zeta}}{12\mu r^2}\right)p_{\theta\dot\gamma}$$
$$+\left(\frac{3h^2h_\theta}{12\mu r^2}\right)p_{\theta\zeta\dot\gamma}+\left(\frac{3h^2h_\zeta}{12\mu r^2}\right)p_{\theta\theta\dot\gamma}+\left(\frac{h^3}{12\mu r^2}\right)p_{\theta\theta\zeta\dot\gamma}=0 \tag{14}$$

where

$$\zeta,\gamma=z,\theta_x,\theta_y,\dot\gamma=\dot z,\dot\theta_x,\dot\theta_y,h_{\zeta_\gamma}=0$$

The second-order dynamic coefficients are determined by solving the previously mentioned Equations (13 and 14) using the finite difference method. The process is illustrated in the following equations:

$$\begin{Bmatrix}F_z^s\\M_x^s\\M_y^s\end{Bmatrix}=\iint_{r,\theta}\left\{p_o+\sum_\zeta p_\zeta\Delta\zeta+\sum_{\dot\zeta}p_{\dot\zeta}\Delta\dot\zeta\right.$$
$$\left.+\frac{1}{2}\sum\nolimits_{\zeta\eta}p_{\zeta\eta}\Delta\zeta\Delta\eta+\sum\nolimits_{\zeta\eta^{\cdot}}p_{\zeta\eta^{\cdot}}\Delta\zeta\Delta\eta^{\cdot}\right\}$$
$$\times\begin{Bmatrix}-1\\r\sin\theta\\-r\cos\theta\end{Bmatrix}r\mathrm{d}r\mathrm{d}\theta=F_o+K_{\eta\zeta}\begin{Bmatrix}\Delta z\\\Delta\theta_x\\\Delta\theta_y\end{Bmatrix}+C_{\eta\zeta}\begin{Bmatrix}\Delta\dot z\\\Delta\dot\theta_x\\\Delta\dot\theta_y\end{Bmatrix}$$
$$+K_{\eta\zeta\gamma}\begin{Bmatrix}0.5\Delta z^2\\0.5\Delta\theta_x^2\\0.5\Delta\theta_y^2\\\Delta z\Delta\theta_x\\\Delta z\Delta\theta_y\\\Delta\theta_x\Delta\theta_y\end{Bmatrix}+C_{\eta\zeta\gamma}\begin{Bmatrix}\Delta z\Delta\dot z\\\Delta z\Delta\dot\theta_x\\\Delta z\Delta\dot\theta_y\\\Delta\theta_x\Delta\dot z\\\Delta\theta_x\Delta\dot\theta_x\\\Delta\theta_x\Delta\dot\theta_y\\\Delta\theta_y\Delta\dot z\\\Delta\theta_y\Delta\dot\theta_x\\\Delta\theta_y\Delta\dot\theta_y\end{Bmatrix} \tag{15}$$

$K_{\eta\zeta\gamma}$ and $C_{\eta\zeta\gamma}$ represent the second-order stiffness and damping matrices, and these matrices can be given as follows:

$$K_{\eta\zeta\gamma}=\begin{bmatrix}K_{zzz}&K_{zz\theta_x}&K_{zz\theta_y}&K_{z\theta_x\theta_x}&K_{z\theta_x\theta_y}&K_{z\theta_y\theta_y}\\K_{\theta_xzz}&K_{\theta_xz\theta_x}&K_{\theta_xz\theta_y}&K_{\theta_x\theta_x\theta_x}&K_{\theta_x\theta_x\theta_y}&K_{\theta_x\theta_y\theta_y}\\K_{\theta_yzz}&K_{\theta_yz\theta_x}&K_{\theta_yz\theta_y}&K_{\theta_y\theta_x\theta_x}&K_{\theta_y\theta_x\theta_y}&K_{\theta_y\theta_y\theta_y}\end{bmatrix}$$
$$=\iint_{r,\theta}\begin{Bmatrix}-1\\r\sin\theta\\-r\cos\theta\end{Bmatrix}\left\{p_{zz}\,p_{z\theta_x}\,p_{z\theta_y}\,p_{\theta_x\theta_x}\,p_{\theta_x\theta_y}\,p_{\theta_y\theta_y}\right\}r\mathrm{d}r\mathrm{d}\theta \tag{16}$$

$$C_{\eta\zeta\gamma}=\begin{bmatrix}C_{zzz}&C_{zz\theta_x}&C_{zz\theta_y}&C_{z\theta_xz}&C_{z\theta_x\theta_x}&C_{z\theta_x\theta_y}&C_{z\theta_yz}&C_{z\theta_y\theta_x}&C_{z\theta_y\theta_y}\\C_{\theta_xzz}&C_{\theta_xz\theta_x}&C_{\theta_xz\theta_y}&C_{\theta_x\theta_xz}&C_{\theta_x\theta_x\theta_x}&C_{\theta_x\theta_x\theta_y}&C_{\theta_x\theta_yz}&C_{\theta_x\theta_y\theta_x}&C_{\theta_x\theta_y\theta_y}\\C_{\theta_yzz}&C_{\theta_yz\theta_x}&C_{\theta_yz\theta_y}&C_{\theta_y\theta_xz}&C_{\theta_y\theta_x\theta_x}&C_{\theta_y\theta_x\theta_y}&C_{\theta_y\theta_yz}&C_{\theta_y\theta_y\theta_x}&C_{\theta_y\theta_y\theta_y}\end{bmatrix}=\iint_{r,\theta}\begin{Bmatrix}-1\\r\sin\theta\\-r\cos\theta\end{Bmatrix}$$
$$\times\left\{p_{zz\cdot}\,p_{z\dot\theta_x}\,p_{z\dot\theta_y}\,p_{\theta_xz^{\cdot}}\,p_{\theta_x\dot\theta_x}\,p_{\theta_x\dot\theta_y}\,p_{\theta_yz^{\cdot}}\,p_{\theta_y\dot\theta_x}\,p_{\theta_y\dot\theta_y}\right\}r\mathrm{d}r\mathrm{d}\theta \tag{17}$$

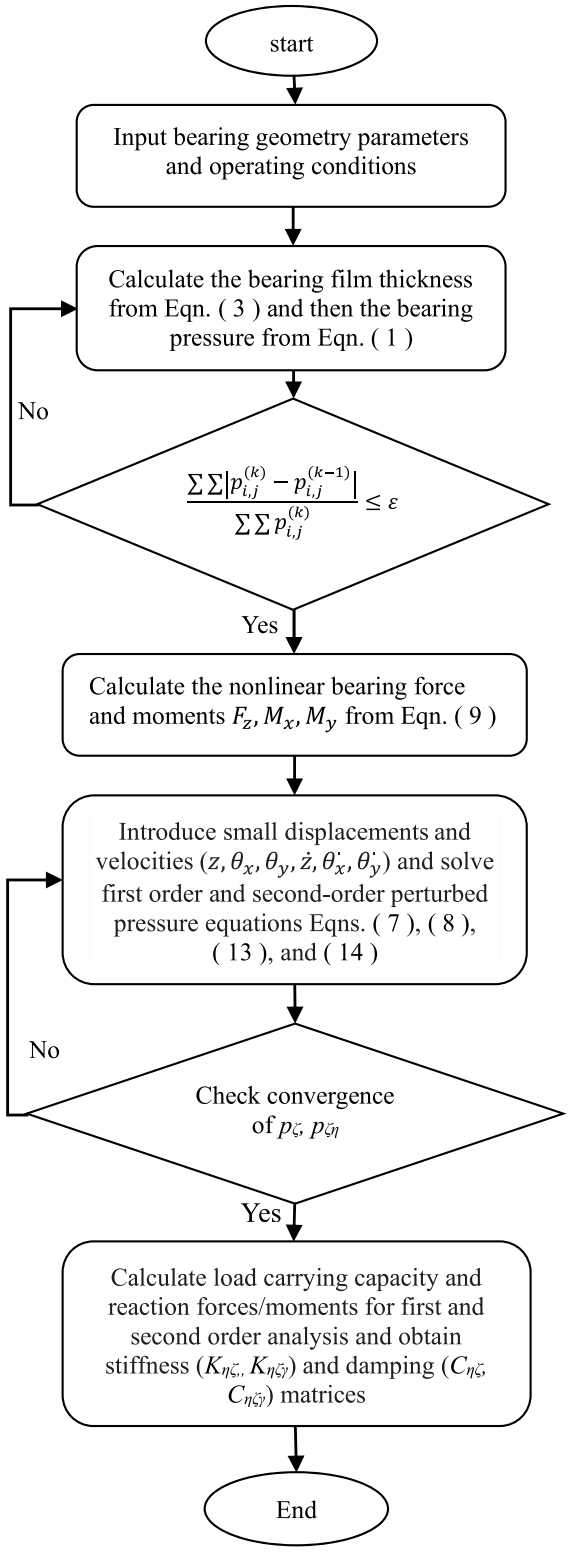

Fig. 3. A flowchart outlines the steps involved in the numerical analysis.

$K_{zzz} = \partial F_z/\partial z^2$, $K_{zz\theta_x} = \partial F_z/\partial z\partial\theta_x$, $K_{z\theta_x\theta_y} = \partial F_z/\partial\theta_x\partial\theta_y$, $K_{\theta_x z\theta_x} = \partial M_x/\partial z\partial\theta_x$, … and so on.

$C_{zzz} = \partial F_z/\partial z\partial\dot{z}$, $C_{zz\theta_x} = \partial F_z/\partial z\partial\dot{\theta_x}$, $C_{\theta_x z\theta_y} = \partial M_x/\partial z\partial\dot{\theta_y}$, $C_{\theta_x zz} = \partial M_x/\partial z\partial\dot{z}$, … and so on.

A computer program was created to analyze the performance characteristics and dynamic behavior of a herringbone-grooved thrust bearing. This program uses data provided in Table 1 to perform the calculations. To solve the complex equations governing pressure distribution within the bearing (Equations 1, 7, 8, 13, and 14), the program incorporates three numerical techniques, the Gauss-Seidel iterative technique, the finite difference method, and the successive over-relaxation technique. By combining these techniques, the program can effectively analyze the thrust bearing's performance and dynamic coefficients. The following flowchart shows the solution steps that were followed to solve the previous equations to obtain the dynamic parameters of the herringbone thrust bearing under study, as shown in Fig. 3. The computational parameters of the herringbone-grooved thrust bearing used in the calculations are listed in Table 3.

3. Results and discussion

In this section, an investigation of the dynamic behavior of the herringbone-grooved thrust bearing by analyzing its stiffness and damping properties was done. An infinitesimal perturbation approach was applied to the Reynolds equation. This approach allowed us to calculate the bearing forces and moments for various levels of misalignment, fluid film thickness, and rotational speed. The analysis focused on how these factors influence the bearing's first-order and second-order dynamic coefficients, which are crucial for understanding its stability and response to external disturbances.

3.1. Validation of the proposed model

To ensure the numerical precision of the model used in this study, the pressure distribution in a nondimensional format is calculated and compared with the findings (Najar & Harmain, 2014) and is presented in Fig. 4. The outcomes obtained in this paper exhibit considerable agreement with those of Najar and Harmain (2014), affirming the validity of the model proposed herein, as depicted in Fig. 4. Subsequently, the model is adjusted and converted

Table 3. Herringbone thrust bearing computational parameters.

Design parameter	Viscosity, μ (N.s/m^2)	Groove depth h_g (m)	Nominal clearance. C [m]	Rotational speed, n (rpm)	Number of grooves, N	Inner radius, r_i (m)	Outer radius, r_0 (m)
Value	0.036	1×10^{-5}	1×10^{-5}	7200	8	2.2×10^{-3}	3.6×10^{-3}

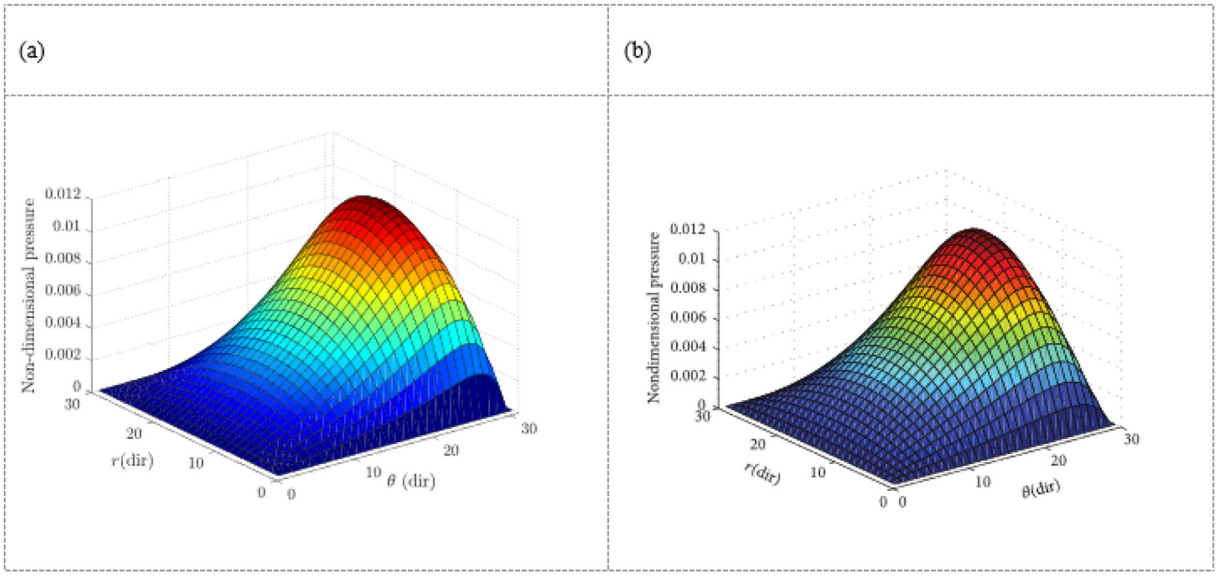

Fig. 4. Nondimensional pressure distribution in radial and circumferential directions: (a) current model and (b) Najar and Harmain (2014).

to dimensional form to investigate the herringbone-grooved thrust bearing, shifting the focus from the inclined pad thrust bearing.

3.2. Force and moments

The analysis of bearing forces and moments in the herringbone thrust bearing using perturbation techniques involves studying the effects of minor displacements and velocities in the steady-state position. This analysis helps in understanding how changes in various parameters impact the performance of the bearing. In this study, three distinct approaches were used to apply perturbations: first-order coefficients, second-order coefficients, and the Reynolds equation. The first-order coefficients (F_{zf}, M_{xf}, M_{yf}) represent the linear terms, while the second-order coefficients (F_{zs}, M_{xs}, M_{ys}) capture the quadratic terms in the perturbation analysis. The Reynolds equation (F_{zRe}, M_{xRe}, M_{yRe}) is a fundamental equation that describes the fluid film behavior in the bearing, as depicted in Table 4. To assess the influence of perturbations on the bearing forces and moments, the fluctuation of these quantities is plotted with respect to the misalignment angle θ_x. By varying the perturbation values, the researchers were able to observe the changes in bearing performance across different perturbation levels.

The relationship between bearing axial force F_z (first column), moment of the x-axis M_x (second column), and moment of the y-axis M_y (last column) is examined in relation to the misalignment angle θ_{x_0}, and is shown in Fig. 5. The study involves three perturbations from the equilibrium position, as outlined in Table 4. The results for each perturbation case are presented in rows, with case (a) in the first row, case (b) in the second row, and case (c) in the third row. Three different methods are used. The first method involves integrating the Reynolds equation, represented by solid lines. The second method uses first-order coefficients and is depicted by dashed lines. The third method uses second-order coefficients and is denoted by dash-dotted lines.

Results in Fig. 5a and b indicate that at small perturbations, the forces evaluated through direct integration are very close to those calculated using the bearing's linear and nonlinear coefficients. However, as the perturbation increases, a larger deviation emerges between the force evaluated directly from the Reynolds equation and the force based on the bearing coefficients. Fig. 5c demonstrates that the force evaluation based on

Table 4. Displacements and velocities used in perturbation analysis.

Case	Δz	$\Delta\theta_x$	$\Delta\theta_y$	$\Delta\dot{z}$	$\Delta\dot{\theta}_x$	$\Delta\dot{\theta}_y$
a	$1\times10^{-4}\times C$	1×10^{-6}	1×10^{-6}	$1\times10^{-4}\times\omega\times C$	$1\times10^{-6}\times\omega$	$1\times10^{-6}\times\omega$
b	$1\times10^{-3}\times C$	1×10^{-5}	1×10^{-5}	$1\times10^{-3}\times\omega\times C$	$1\times10^{-5}\times\omega$	$1\times10^{-5}\times\omega$
c	$1\times10^{-2}\times C$	1×10^{-4}	1×10^{-4}	$1\times10^{-2}\times\omega\times C$	$1\times10^{-4}\times\omega$	$1\times10^{-4}\times\omega$

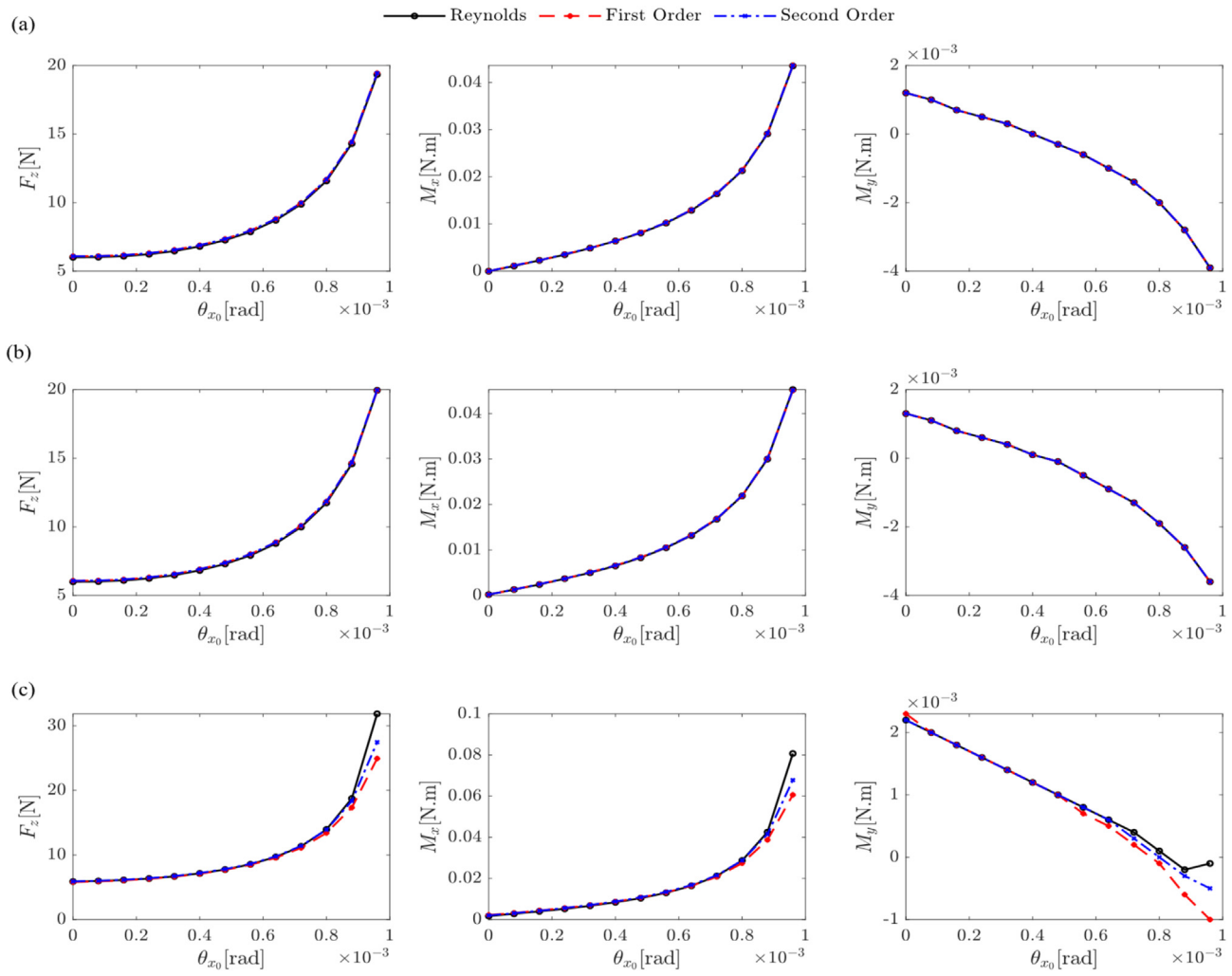

Fig. 5. Relationship between bearing force and moments with eccentricity ratio at different perturbation values.

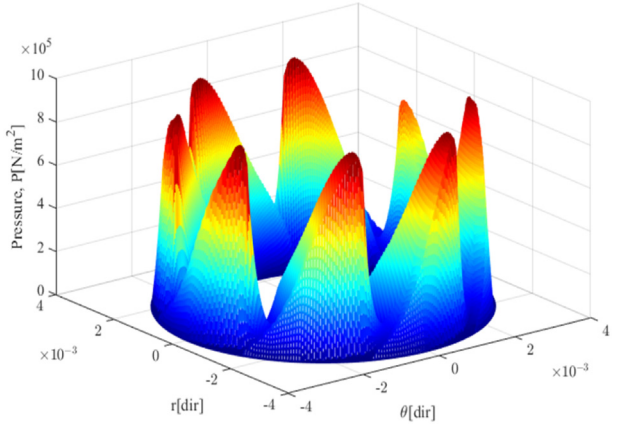

Fig. 6. Pressure distribution for aligned HGTB. HGTB, herringbone-grooved thrust bearing.

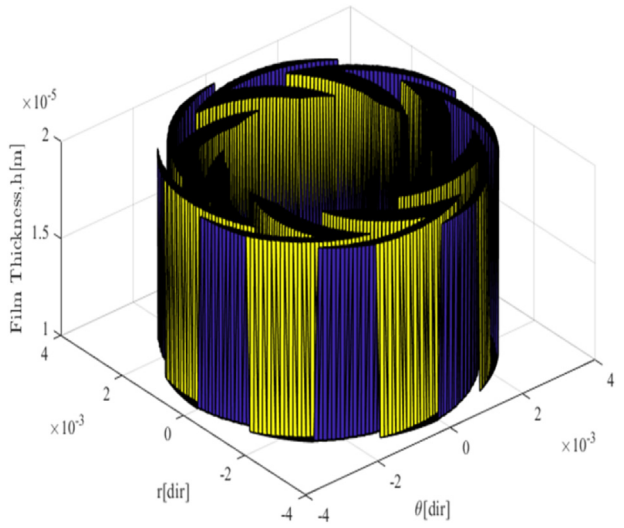

Fig. 7. Fluid film distribution for aligned HGTBs. HGTB, herringbone-grooved thrust bearing.

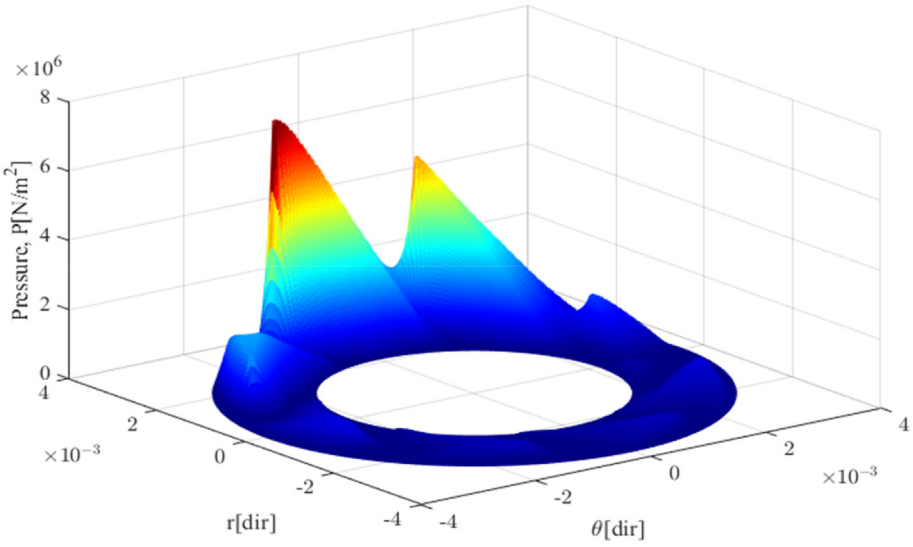

Fig. 8. Pressure distribution for misaligned bearing at $\theta_{x_0} = 0.24 \times 10^{-3}$ rad.

the second-order bearing coefficients provides a better approximation of the nonlinear force compared with the first-order bearing coefficients across most of the bearing's operational range. This indicates that the inclusion of higher order terms has a more significant impact on the bearing forces and moments as the perturbation level rises.

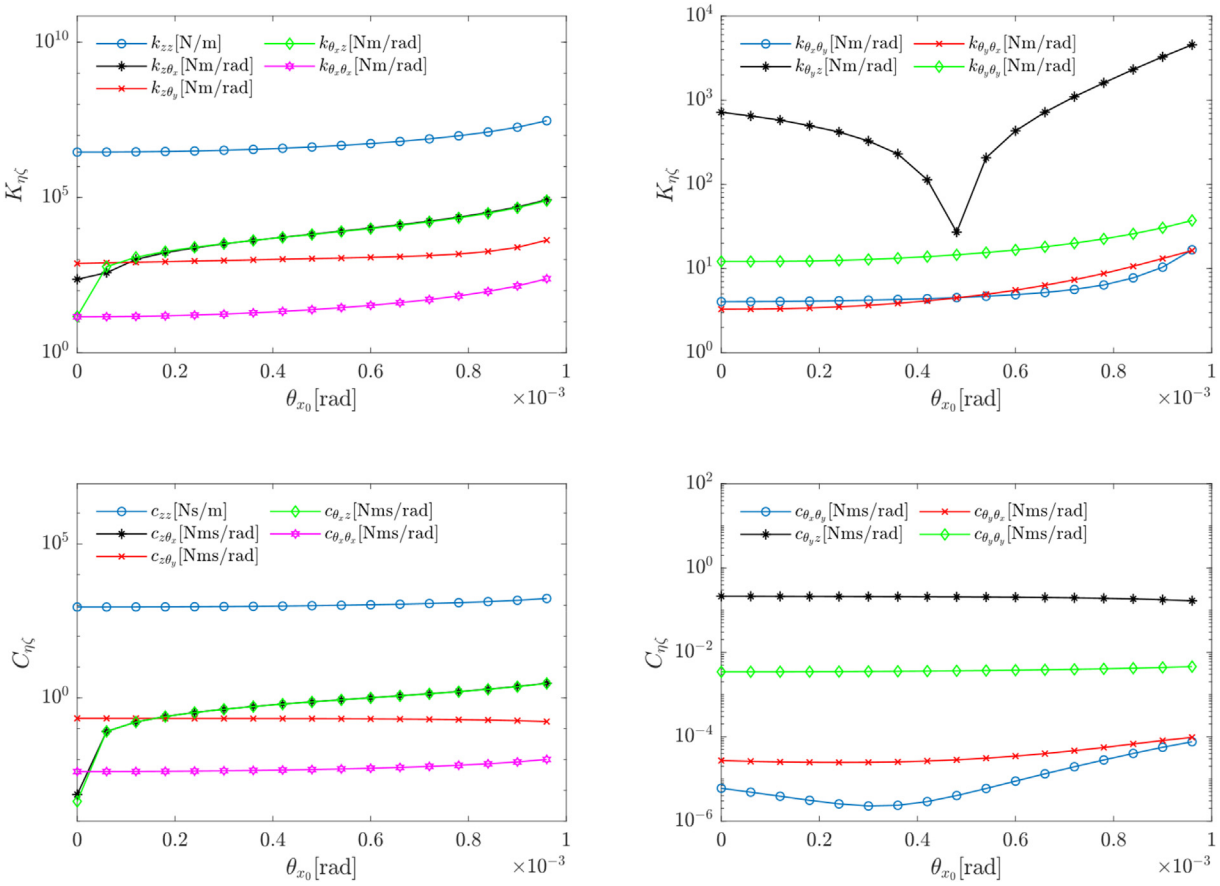

Fig. 9. First-order dynamic coefficient variation with misalignment angle θ_{x_0}.

3.3. Herringbone-grooved thrust bearing pressure and film thickness

The herringbone-grooved thrust bearing parameters are calculated using the infinitesimal perturbation approach with the assumption of small perturbations in the displacement and velocity, and the shaft is assumed to have misalignment θ_x in x direction only. The bearing dynamic coefficients were obtained under various operating conditions, such as misalignment angle θ_{x_0} and rotating speed n. As indicated in a previous study (Elsayed *et al.*, 2023), the effect of mesh size on the bearing dynamic coefficients was examined, revealing that its impact is negligible for mesh sizes smaller than 30 × 120. Thus, a mesh size of 30 × 120 was chosen for these calculations to optimize computational efficiency. The pressure distribution and film thickness for the herringbone-aligned bearing are shown in Figs. 6 and 7. Fig. 6 illustrates a uniform pressure distribution over the bearing pad when the misalignment angle θ_x is zero, with a maximum pressure value of 9.29×10^5 N/m^2. Fig. 7 highlights the film thickness in the grooved area, with yellow areas indicating the groove depth, and a maximum film thickness of 2×10^{-5} m.

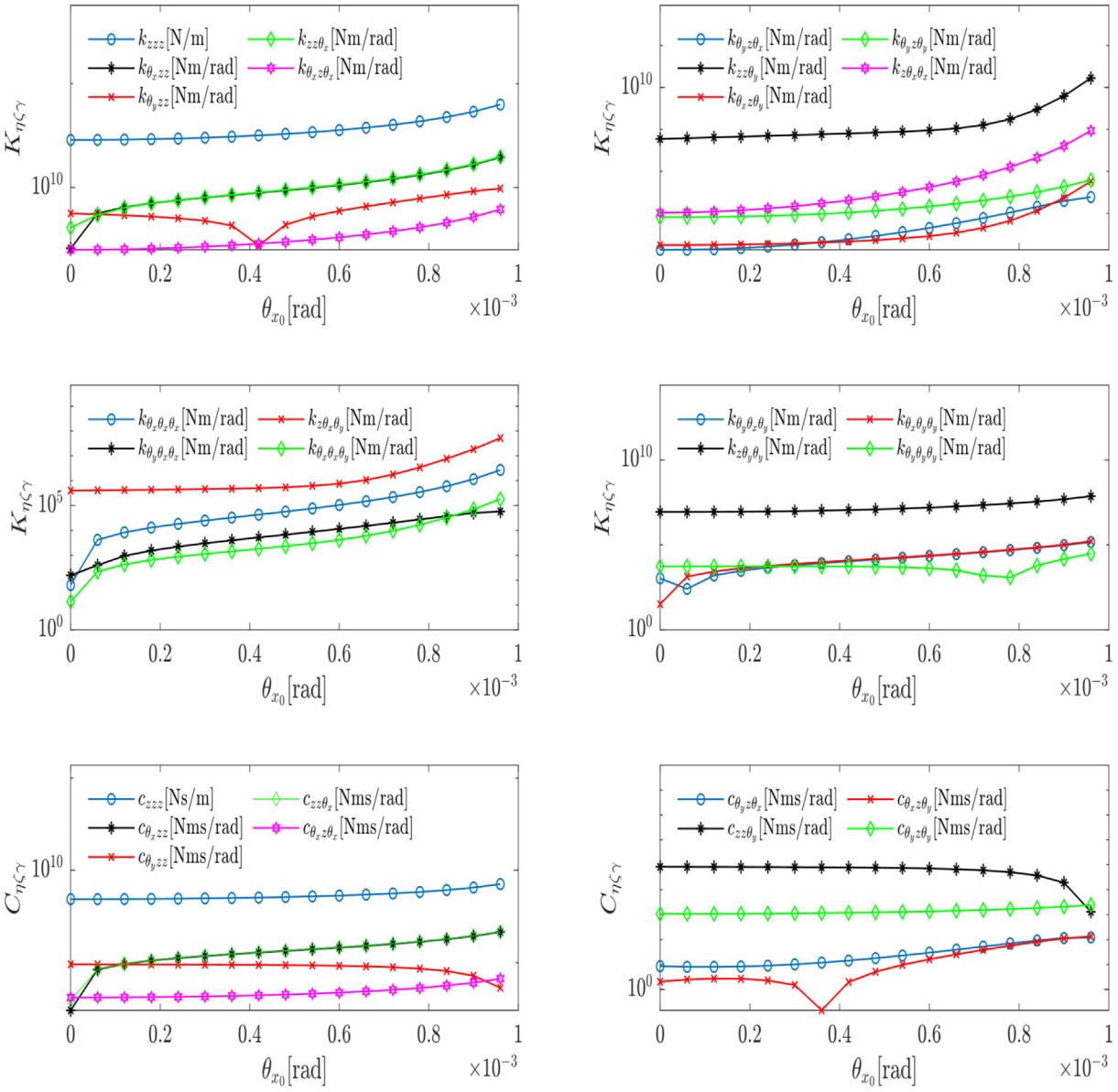

Fig. 10. Second-order dynamic coefficient variation with misalignment angle θ_{x_0}.

3.4. Effect of misalignment θ_{x_0} on bearing coefficients

The bearing stiffness and damping coefficients for the herringbone-grooved thrust bearing are obtained from the integration of the perturbed pressure equations over the bearing area (Equations 11, 12, 16, 17). In the first-order analysis, there are nine stiffness and nine damping coefficients, and 18 s-order coefficients and 27 damping coefficients, of which only nine have values. The pressure distribution for a misaligned bearing is shown in Fig. 8, when the shaft is allowed to have a tilt around the x-axis, which shows nonuniform pressure distribution around the bearing pad due to the tilting effect and the largest value of the pressure is 6.944×10^6 N/m^2.

Figs. 9 and 10 show the relationship between the change in dynamic parameters and the angle of misalignment of the bearing at $C = 1 \times 10^{-5}$ m, $n = 7200$ rpm, and $N = 8$ grooves, when θ_{x_0} changes from 0 to 0.96×10^{-3} rad. The graphs show the strength of the bearing's response to various movements (represented by bearing coefficients). Fig. 9 displays the effects of misalignment on the main stiffness and damping properties (first-order dynamic coefficients). Most of these properties become stronger as the misalignment angle increases. However, some properties, like $[C_{z\theta_x} = C_{\theta_x z}]$, remain constant and $K_{\theta_y z}$ decrease with the increase in the misalignment angle until the misalignment angle be 0.48×10^{-3} rad and begins to increase again.

Fig. 10 shows the relationship between the second-order bearing dynamic coefficients and the misalignment angle. Like the first-order coefficients, most coefficients increase with misalignment. There are also some coefficients, like $[C_{zz\theta_x} = C_{\theta_x zz}]$, that do not change with the angle. Stiffness coefficients $K_{\theta_y zz}$ decrease until θ_x equals 0.42×10^{-3} rad and increase again; also, $C_{\theta_x z\theta_y}$ has its smallest value at θ_x equaling 0.36×10^{-3} rad.

3.5. Effect of rotational speed n on bearing coefficients

The effect of changing the rotational speed on the first-order and second-order dynamic coefficients of a herringbone-grooved thrust bearing was also

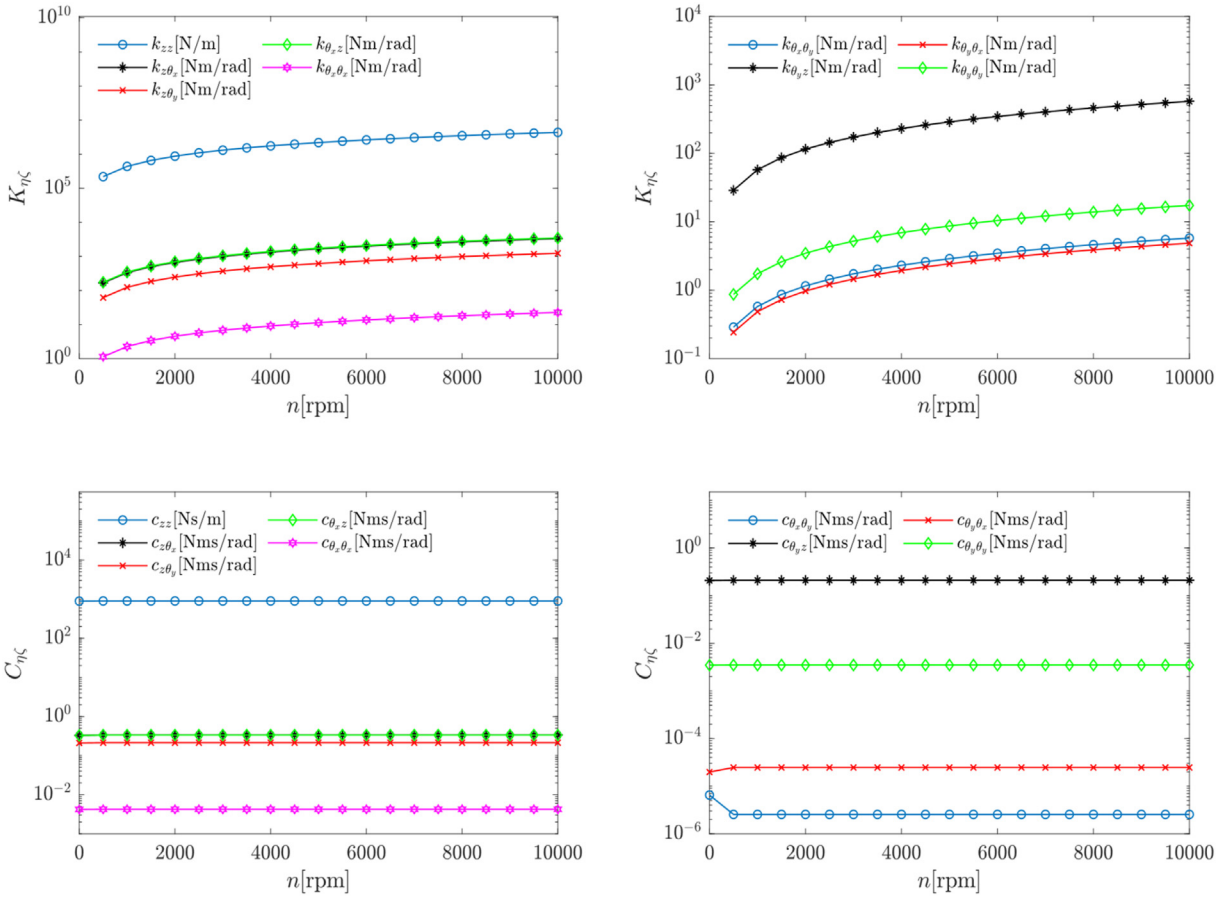

Fig. 11. First-order dynamic coefficients variation with rotational speed n.

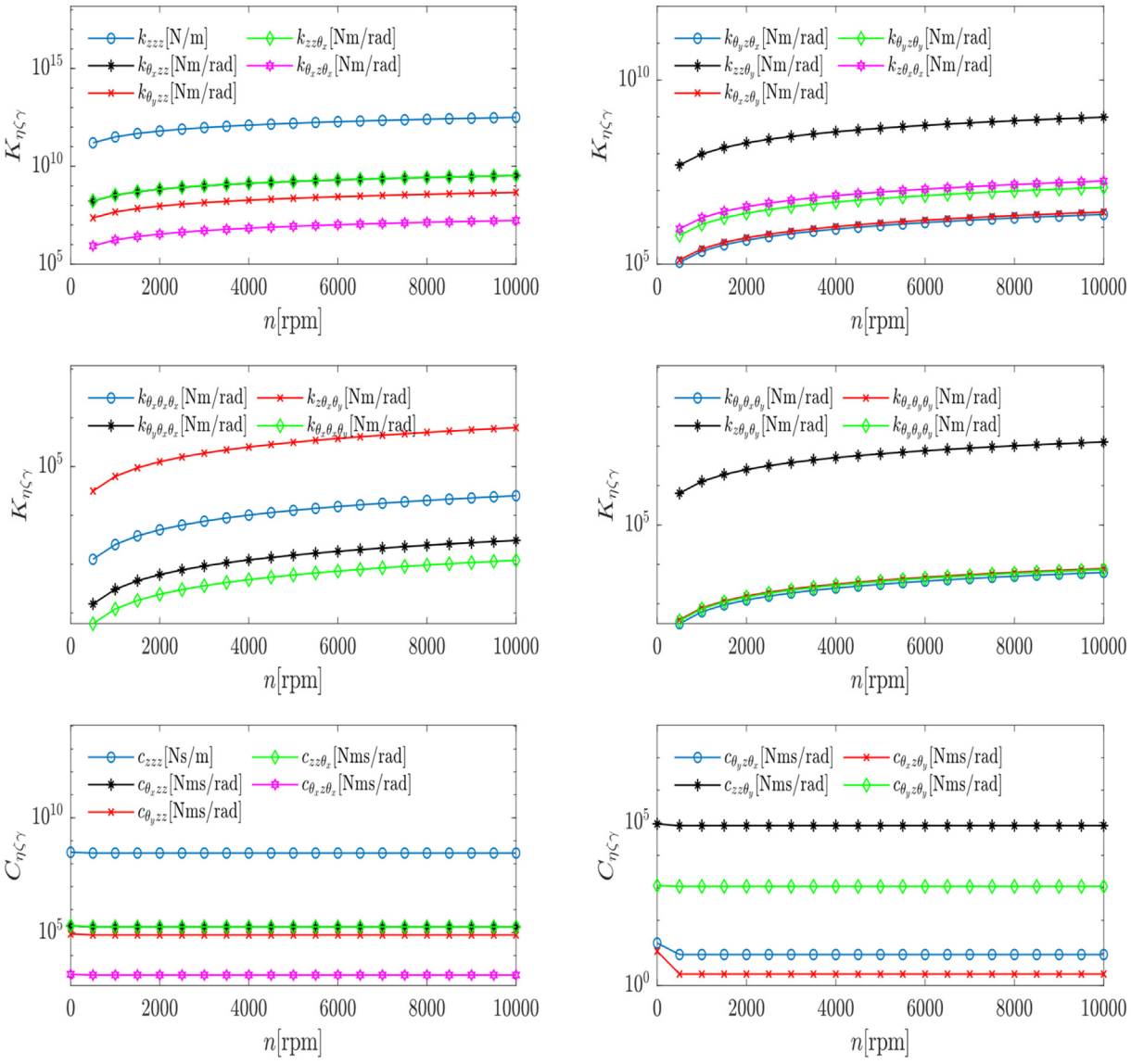

Fig. 12. Second-order dynamic coefficients variation with rotational speed n.

studied when the rotational speed changed from 0 to 10,000 rpm, when all other variables were held constant ($\theta_{x_0} = 0.24 \times 10^{-3}$ rad $C = 1 \times 10^{-5}$ m, $n = 7200$ rpm, $N = 8$ grooves), as shown in Figs. 11 and 12. The change of the first-order stiffness and damping coefficients with rotational speed change is illustrated in Fig. 11, which shows that as the rotational speed increases, the value of the stiffness coefficients increases with it, while the damping coefficients remain almost constant with the change in rotational speed. It was also found that $C_{z\theta_x} = C_{\theta_x z}$, and K_{zz} and C_{zz} have the largest values, and $K_{\theta_y\theta_x}$ and $C_{\theta_x\theta_y}$ are the smallest among all the coefficients. Fig. 12 illustrates the relationship between the second-order dynamic coefficients (stiffness and damping) and the rotational speed change. As clear from the figure, as rotational speed increases, the stiffness coefficient value increases, and K_{zzz} is the largest stiffness coefficients, while $K_{\theta_y\theta_x\theta_y}, K_{\theta_x\theta_x\theta_y}, K_{\theta_x\theta_y\theta_y}, K_{\theta_y\theta_y\theta_y}$ are the least valuable among the stiffness coefficients. The damping coefficient value remains approximately constant as the rotational speed increases and $C_{zz\theta_x} = C_{\theta_x zz}$, with C_{zzz} being the largest value and $C_{\theta_x z\theta_y}$ the least.

3.6. Conclusions

In this paper, the flow within the fluid film of a herringbone-grooved thrust bearing between the runner and the bearing is modeled by numerically solving the two-dimensional Reynolds equation using the finite difference method. To calculate the

forces and moments of the bearing, the infinitesimal perturbation method is used, introducing a small angular misalignment in the x-direction. The first-order and second-order dynamic coefficients are then evaluated. The study investigates the influence of misalignment and rotational speed on the dynamic coefficients of the bearing. Through the analysis, several significant conclusions are drawn, including:

(1) The force and moment calculated using three different methods (based on the Reynolds equation, the first-order, and the second-order coefficients) are nearly identical. This remarkable similarity serves as an indication of the accuracy and validity of the calculation methods used in the study. It provides confidence in the correctness of the chosen approach and reinforces the reliability of the obtained results.
(2) When the rotor is aligned, the max pressure is 9.29 bar and when the rotor tilted by 0.24×10^{-3} rad, the max pressure increased to 69.44 bar As the misalignment angle increases, the pressure also increases, causing an increase in the load-carrying capacity and bearing coefficients.
(3) The first-order and second-order dynamic coefficients increase with the increase in the misalignment angle, and the misalignment angle has a more intricate and nonlinear impact on the bearing coefficients.
(4) The bearing first-order and second-order stiffness coefficients increase linearly with rotational speed, while the rotational speed does not impact the damping coefficients.

These conclusions shed light on the behavior and performance of the herringbone-grooved thrust bearing under different operating conditions, providing valuable insights for the design and optimization of such systems.

Author contribution

EE wrote the first draft of the manuscript. EE did the investigation. HS revise the research MATLAB codes. TE and HS supervise the research. All authors revised the final version.

Funding

The authors did not receive any funding for this research.

Ethics information

Not Applicable.

Conflict of interest

The authors declare that they have no conflict of interest.

References

Agrawal, N., & Sharma, S. C. (2023). Micro-grooved hybrid spherical thrust bearing with Non-Newtonian lubricant behaviour. *International Journal of Mechanical Sciences, 240*, Article 107940.

Ahmed, O., El-Sayed, T., & Sayed, H. (2023). Finite element analyses of rotor/bearing system using second-order journal bearings stiffness and damping coefficients. *Journal of Vibration and Control*, Article 10775463231204388.

Ahmed, O., Sayed, H., & El-Sayed, T. A. (2024). Dynamic analysis and experimental verification of flexible unbalance rotor supported by two identical journal bearings. *Trends Adv Sci Technol, 1*, 11.

Dai, H., Xiang, G., Wang, J., Guo, J., Wang, C., & Jia, H. (2022). Study on time-varying mixed lubrication performance of microgroove journal-thrust coupled bearing under water lubrication. *Industrial Lubrication & Tribology, 74*, 265–273.

El-Sayed, T., Friswell, M. I., & Sayed, H. (2023). Approximating fluid bearing characteristics using polynomials for the nonlinear dynamics of rotating machines. *Tribology International*, Article 108669.

El-Sayed, T. A., & Sayed, H. (2022). Bifurcation analysis of rotor/bearing system using third-order journal bearing stiffness and damping coefficients. *Nonlinear Dynamics, 107*, 123–151.

El-Sayed, E. K., Sayed, H., & El-Sayed, T. A. (2024). Analysis of second-order thrust bearing coefficients considering misalignment effect. *Journal of Vibration Engineering & Technologies, 12*, 1957–1977.

Hu, Y., & Meng, Y. (2019). Theoretical and experimental study of transient behavior of spiral-groove thrust bearings during start-up. *Tribology Transactions, 63*, 154–172.

Jang, G., & Kim, Y. (1999). *Calculation of dynamic coefficients in a hydrodynamic bearing considering five degrees of freedom for a general rotor-bearing system.*

Jang, G., & Lee, S. (2006). Determination of the dynamic coefficients of the coupled journal and thrust bearings by the perturbation method. *Tribology Letters, 22*, 239–246.

Jang, G., Lee, S., Kim, H., & Kim, C. (2005). Dynamic analysis of a HDD spindle system with FDBs due to the bearing width and asymmetric grooves of journal bearing. *Microsystem Technologies, 11*, 499–505.

Jang, G., & Yoon, J. W. (2003). Stability analysis of a hydrodynamic journal bearing with rotating herringbone grooves. *Journal of Tribology - Transactions of the ASME, 125*, 291–300.

Lehn, A., & Schweizer, B. (2016). Generalized Reynolds equation for fluid film problems with arbitrary boundary conditions: Application to double-sided spiral groove thrust bearings. *Archive of Applied Mechanics, 86*, 743–760.

Lin, X., Wang, S., Jiang, S., & Zhang, S. (2022). Dynamic characteristics of high-speed water-lubricated spiral groove thrust bearing based on turbulent cavitating flow lubrication model. *Chinese Journal of Mechanical Engineering, 35*, 1–21.

Lin, X., Wang, R., Zhang, S., & Jiang, S. (2020). Study on dynamic characteristics for high speed water-lubricated spiral groove thrust bearing considering cavitating effect. *Tribology International, 143*, Article 106022.

Luan, W., Liu, Y., Wang, Y., & Xu, F. (2023). Effect of herringbone groove structure parameters on the static performance of gas foil herringbone groove thrust bearings. *Tribology International, 177*, Article 107979.

Najar, F. A., & Harmain, G. A. (2014). Numerical investigation of pressure profile in hydrodynamic lubrication thrust bearing. *International Scholarly Research Notices, 2014*, 157615.

Oh, S.-M., & Rhim, Y.-C. (2001). The numerical analysis of spindle motor bearing composed of herringbone groove journal and

spiral groove thrust bearing. *KSME International Journal, 2*, 93–102.
Ran, H., Dai, P., Yan, S., Wang, F., Yao, X., Wang, J., & Zuo, G. (2022). Flow mechanisms and lubrication performance of water-lubricated thrust bearings with herringbone grooves. *Lubricants, 10*, 182.
Sahu, M., Sarangi, M., & Majumdar, B. C. (2006). Thermo-hydrodynamic analysis of herringbone grooved journal bearings. *Tribology International, 39*, 1395–1404.
Sayed, H., & El-Sayed, T. (2022a). A novel method to evaluate the journal bearing forces with application to flexible rotor model. *Tribology International, 173*, Article 107593.
Sayed, H., & El-Sayed, T. A. (2022b). Nonlinear dynamics and bifurcation analysis of journal bearings based on second order stiffness and damping coefficients. *International Journal of Non-Linear Mechanics, 142*, Article 103972.
Sayed, H., El-Sayed, T. A., & Friswell, M. (2023). Continuation analysis of rotor bearing systems through direct solution of Reynolds equation. In *Advances in machinery, materials science and engineering application IX* (pp. 217–222). IOS Press.
Schlums, H., Hühne, C., & Sinapius, M. (2022). Design of a herringbone-grooved bearing for application in an electrically driven air compressor. *Machines, 10*, 662.
Tang, D.-X., Yin, L., Xiao, B., Han, Y.-F., Xiang, G., & Wang, J.-X. (2022). Numerical analysis on mixed lubrication performance of journal-thrust coupled microgroove bearings with different bottom shapes. *J Central South Univ, 29*, 1197–1212.
Wang, C.-C., & Lin, J.-T. (2022). Numerical study of hydrodynamic herringbone-grooved journal bearings combined with thrust bearings considering thermal effects. *Journal of Mechanisms, 38*, 13–21.
Wang, J., Ran, H., Dai, P., Yan, S., Yao, X., Wang, F., & Zuo, G. (2022). Flow characteristic analysis of a herringbone groove thrust bearing with shaft misalignment. *Industrial Lubrication & Tribology, 75*, 67–73.
Xiang, G., & Han, Y. (2020). Study on the tribo-dynamic performances of water-lubricated microgroove bearings during start-up. *Tribology International, 151*, Article 106395.
Xiang, G., Han, Y., Chen, R., Wang, J., Ni, X., & Xiao, K. (2020). A hydrodynamic lubrication model and comparative analysis for coupled microgroove journal-thrust bearings lubricated with water. *Proc Inst Mech Eng J Eng Tribol, 234*, 1755–1770.
Xiang, G., Han, Y., Wang, J., Xiao, K., & Li, J. (2019). A transient hydrodynamic lubrication comparative analysis for misaligned micro-grooved bearing considering axial reciprocating movement of shaft. *Tribology International, 132*, 11–23.
Xiang, G., Han, Y., Wang, J., Xiao, K., & Li, J. (2021). Influence of axial microvibration on the transient hydrodynamic lubrication performance of misaligned journal–thrust microgrooved coupled bearings under water lubrication. *Tribology Transactions, 64*, 579–592.
Xiang, G., Wang, J., Zhou, C., Shi, Y., Wang, Y., Cai, J., et al. (2021b). A tribo-dynamic model of coupled journal-thrust water-lubricated bearings under propeller disturbance. *Tribology International, 160*, Article 107008.
Yu, Y., Pu, G., & Jiang, K. (2017). Modeling and analysis of the static characteristics and dynamic responses of herringbone-grooved thrust bearings. *IOP Conference Series: Materials Science and Engineering, 280*, 012006.
Yu, Y., Pu, G., Jiang, T., & Jiang, K. (2021). Optimization of herringbone grooved thrust air bearings for maximum load capacity. *Journal of Tribology, 143*, Article 121805.
Zhang, S., Jiang, S., & Lin, X. (2020). Static and dynamic characteristics of high-speed water-lubricated spiral-groove thrust bearing considering cavitating and centrifugal effects. *Tribology International, 145*, Article 106159.
Zhou, G., Li, R., Liao, D., Yang, W., & Zhong, P. (2023). Lubrication structure design of water lubricated rubber thrust bearing with spiral groove for shaftless rim driven thruster. *Tribology International, 178*, Article 108098.